



**HAL**  
open science

# Investigation on mechanical properties of tribofilm formed on Ti–6Al–4V surface sliding against a DLC coating by nano-indentation and micro-pillar compression techniques

H.H. Ding, V. Fridrici, G. Guillonneau, S. Sao-Joao, J. Geringer, Julien Fontaine, Ph Kapsa

## ► To cite this version:

H.H. Ding, V. Fridrici, G. Guillonneau, S. Sao-Joao, J. Geringer, et al.. Investigation on mechanical properties of tribofilm formed on Ti–6Al–4V surface sliding against a DLC coating by nano-indentation and micro-pillar compression techniques. *Wear*, 2019, 432-433, pp.202954. 10.1016/j.wear.2019.202954 . hal-02383587

**HAL Id: hal-02383587**

**<https://hal.science/hal-02383587>**

Submitted on 25 Oct 2021

**HAL** is a multi-disciplinary open access archive for the deposit and dissemination of scientific research documents, whether they are published or not. The documents may come from teaching and research institutions in France or abroad, or from public or private research centers.

L'archive ouverte pluridisciplinaire **HAL**, est destinée au dépôt et à la diffusion de documents scientifiques de niveau recherche, publiés ou non, émanant des établissements d'enseignement et de recherche français ou étrangers, des laboratoires publics ou privés.



Distributed under a Creative Commons Attribution - NonCommercial 4.0 International License

# Investigation on mechanical properties of tribofilm formed on Ti–6Al–4V surface sliding against a DLC coating by nano-indentation and micro-pillar compression techniques

H.H. Ding<sup>1,3</sup>, V. Fridrici<sup>1\*</sup>, G. Guillonneau<sup>1</sup>, S. Sao-Joao<sup>2</sup>, J. Geringer<sup>2</sup>, J. Fontaine<sup>1</sup>, Ph. Kapsa<sup>1</sup>

*1. Laboratoire de Tribologie et Dynamique des Systèmes, UMR CNRS 5513 ECL-ENISE-ENTPE, Université de Lyon, Ecole Centrale de Lyon, Bat. TMM23, 36 avenue Guy de Collongue, 69134 Ecully cedex, France*

*2. Université de Lyon, IMT Mines Saint-Etienne, Centre CIS, INSERM, SainBioSE, F - 42023 Saint-Etienne, France*

*3. Tribology Research Institute, State Key Laboratory of Traction Power, Southwest Jiaotong University, Chengdu, 610031, China*

**Abstract:** A tribofilm was formed on the Ti–6Al–4V surface when sliding against a DLC coating under fretting condition in air. The tribofilm is mainly composed of the oxidized wear product of Ti–6Al–4V alloy. The mechanical properties of the tribofilm and the Ti–6Al–4V alloy were characterized using nano-indentation and micro-pillar compression techniques. From nano-indentation testing, the hardness of tribofilm ( $10 \pm 0.4$  GPa) was 2.6 times higher than that of Ti–6Al–4V alloy ( $3.9 \pm 1.5$  GPa). The reduced Young's modulus of tribofilm ( $170 \pm 3$  GPa) was around 1.3 times higher than that of Ti–6Al–4V alloy ( $130 \pm 30$  GPa). From micro-pillar compression testing, the compression modulus of tribofilm (around 160 GPa) was 2.5–3.3 times higher than that of Ti–6Al–4V alloy (47–62 GPa). The yield strength of tribofilm (around 6.4 GPa) measured by micro-pillar compression, was 6.7–7.1 times higher than that of Ti–6Al–4V alloy (0.90–0.95 GPa). When measuring the hardness on the tribofilm, micro-pillar compression tests could obtain more accurate values than the nano-indentation tests.

**Keywords:** Tribofilm; Micro-pillar compression; Nano-indentation; Ti–6Al–4V; Diamond-like carbon coating

## 1. Introduction

Diamond-like carbon (DLC) coatings are widely used as tribological coatings on metallic components in sliding [1–3]. The friction coefficient of DLC coatings is dependent on many factors [4], such as the environmental condition [5], the deposition technique, which determines their structure [6], etc. In general, a precondition for low friction is the absence of strong bonds, i.e., the reduction of shear strength (Y) between the sliding surfaces. Three processes have a main contribution to the reduction of shear strength during friction: (1) rehybridization with the structural transition of  $sp^3$  to  $sp^2$  on the rubbed DLC coating surface [5,7,8]; (2) passivation of the DLC coating surface during sliding [9,10]; and (3) tribofilm

---

\*Corresponding author. Tel: +33 472 18 62 90.  
E-mail address: [vincent.fridrici@ec-lyon.fr](mailto:vincent.fridrici@ec-lyon.fr) (V. Fridrici).

formation on the rubbed countersurface [1,5,11,12]. Concerning the tribofilms, they are generally produced by a complex process during sliding [13]. Specifically, the wear debris particles are trapped at the contact interfaces and undergo severe deformation as well as chemical reaction with the species from the surroundings [13].

Ti-6Al-4V alloys are widely used in many applications, such as aeronautical industry [14,15] and prosthetic implants [16,17]. However, Ti-6Al-4V / Ti-6Al-4V contacts presented poor tribological performance, including high friction and severe adhesive wear under fretting conditions [15,18]. Thus, DLC coatings could be introduced into Ti-6Al-4V / Ti-6Al-4V contacts. In previous works [19,20], the Ti-6Al-4V / DLC coating contact exhibited low friction coefficient (around 0.2) after the running-in period, and a tribofilm is formed on the Ti-6Al-4V surface. The contact changed from Ti-6Al-4V / DLC coating to tribofilm / DLC coating.

Furthermore, it is well known that the friction coefficient of a contact is influenced by the surface mechanical properties of the contact bodies [4]. The aim of this study is to investigate the mechanical properties of the tribofilm created by friction and wear processes on Ti-6Al-4V surface when sliding against a DLC coating.

Nano-indentation and micro-pillar compression have emerged as two common techniques to investigate the mechanical properties of small volumes [21]. Nano-indentation is a widely applied technique to measure the material's surface hardness ( $H$ ) and reduced Young's modulus ( $E^*$ ) [22–24]. In particular, the continuous stiffness measurement mode (CSM) allows a continuous measurement of the hardness and the Young's modulus as a function of the indentation depth [24,25]. However, nano-indentation testing has two drawbacks: (1) “indentation size effect” which manifests itself in nano-hardness values which decrease with increasing indentation depth [26]; (2) “substrate effect”, i.e., superposition of film and substrate hardness with increasing indentation depth [27]. Micro-pillar compression is a relatively novel technique, which allows to perform the direct measurement of the stress–strain curve of the pillar [28]. The compression device is generally placed within a scanning electron microscope (SEM), which allows *in situ* observation of the deformation of the pillar [29]. The main drawback of micro-pillar compression lies in the additional effort for pillar preparation [30]. Generally, pillars are produced using a focused ion beam (FIB) which **might** induce a thermally affected zone at the pillar edge. Also, the pillar misalignment with the flat punch makes the reduced Young's modulus calculation more difficult. Micro-pillar compression has already been used to characterize interfacial materials like Cu, VN, TiN and W coatings [27], tribologically transformed structure (TTS) [28,31], glaze layer (compacted

interfacial debris) [30], as well as worn surfaces of pure nickel [21] and aluminum–silicon alloys [32]. But, this technique has not been applied to measure the mechanical properties of tribofilm formed on the Ti–6Al–4V alloy when sliding against the DLC coating.

In this paper, a tribofilm was created on the Ti–6Al–4V surface by sliding against a DLC coating surface using a fretting-wear rig. Then, nano-indentation and micro-pillar compression tests were performed on both the tribofilm material and the virgin Ti–6Al–4V surface, in order to compare their mechanical properties. Meanwhile, the results from nano-indentation and micro-pillar compression tests were compared.

## 2. Tribofilm production

### 2.1. Tribological test

The tribofilm was created on a Ti–6Al–4V flat, which slid against a DLC coated Ti–6Al–4V cylinder, using a fretting-wear test rig already described elsewhere [19]. The schematic outline of the fretting-wear test rig and the geometry of the flat and cylinder samples are shown in Fig.1. **The flat and cylinder samples were used to mimic the neck adapter and the femoral stem of the modular hip implant [19].** The flat moved up and down with a displacement amplitude of  $\pm 20 \mu\text{m}$ , and rubbed against the stationary cylinder under a normal force of 250 N (leading to a maximum contact pressure of 316 MPa, **as estimated without considering the surface irregularities**). **The displacement and contact pressure between flat and cylinder samples were adopted according to the results of finite element modeling of the real parts in previous works [33,34].** The frequency was 5 Hz. The number of cycles was 100 000. The fretting test was conducted under ambient atmosphere (temperature: 18–23 °C, humidity: 30–50%).

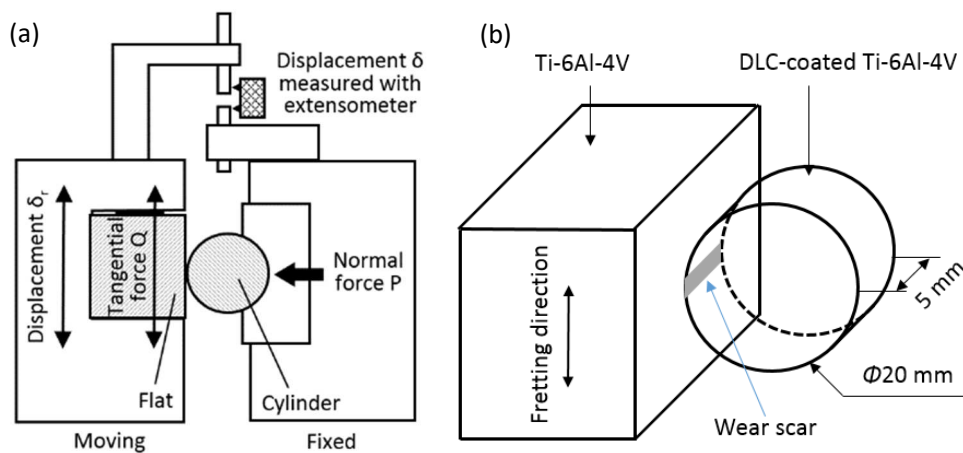


Fig. 1. (a) Schematic outline of the fretting-wear rig and (b) geometry of the flat and the cylinder samples.

The surfaces of flat and cylinder samples were machined by milling, as shown in Fig. 2.

Textured surfaces were adopted in this study according to the real neck adapter and the femoral stem surfaces. The values of the roughness parameter for the flat and cylinder samples were close to those obtained from the neck adapter and the femoral stem [19]. The surface roughness ( $S_a$ ) of flat was around 400 nm, and the surface roughness ( $S_a$ ) of cylinder was around 750 nm. The DLC coating deposition had no significant influence on the surface roughness. The sliding direction for subsequent fretting test is indicated on the surfaces.

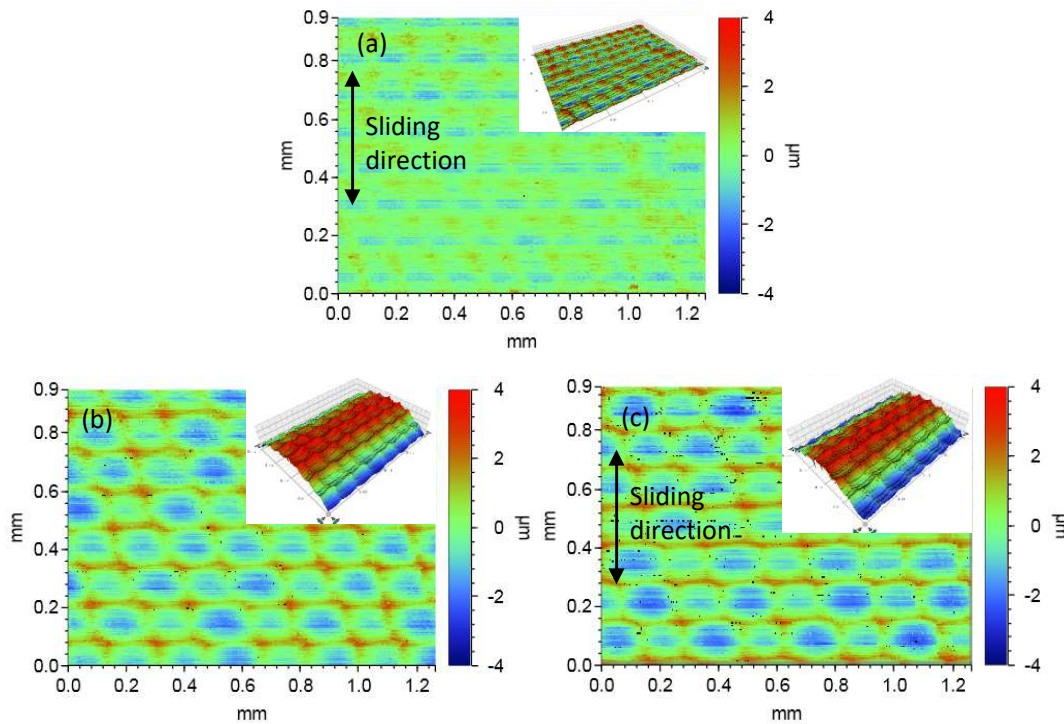


Fig. 2. 3D topography (a) Ti-6Al-4V flat, (b) uncoated Ti-6Al-4V cylinder, and (c) DLC coated cylinder.

The DLC coating was deposited on the cylinder sample using the plasma-assisted chemical vapor deposition (PACVD) technique with the machine TSD 550, from HEF [35]. A Si-rich interlayer with the thickness of approximately  $0.5 \mu\text{m}$  is present as a bonding layer for gradual transition stress, thus enhancing the adhesion between the DLC coating and the Ti-6Al-4V substrate. The produced DLC coating was a-C:H (hydrogenated amorphous carbon film) with approximately 20 at.% of hydrogen [20]. This DLC coating is a commercially available coating in France. The hydrogen content was determined by the deposition process which had already been optimized for tribological applications. In order to facilitate the analysis of DLC coating, it was also deposited on rough (Fig. 2a) and smooth ( $S_a \approx 20 \text{ nm}$ ) flat samples with the same deposition processes. The cross section of the DLC coated rough flat is shown in Fig.3. The DLC coating is continuous with a constant thickness of approximately  $2.0 \mu\text{m}$ .

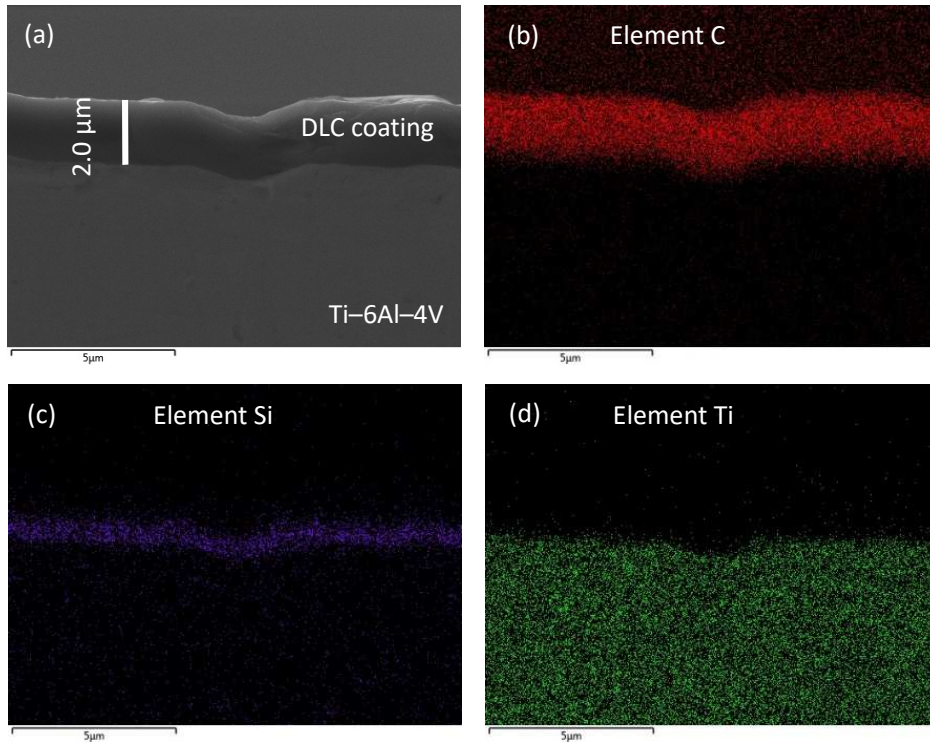


Fig. 3. SEM and EDX observations of the cross section of a DLC coated flat sample: (a) SEM of the cross section of the DLC coated flat; (b) element C; (c) element Si; and (d) element Ti.

To measure the mechanical properties of the DLC coating and the Ti-6Al-4V substrate, nano-indentation tests (Nano Indenter XP, MTS, equipped with a Berkovich diamond tip) were performed on a DLC coated smooth flat and on an uncoated smooth Ti-6Al-4V flat, using the continuous stiffness measurement method (CSM). During CSM, a small displacement oscillation (1 nm) at a given frequency during the indentation test (32 Hz) was superimposed on the indentation motion. This led to a succession of micro-loading-unloading phases, which allowed the measurement of the stiffness of the contact. Loading phase involved elastic and plastic deformation, while unloading involved only elastic deformation, and thus allowed to compute the stiffness as the initial slope of the unloading part of the force-displacement curve. Therefore, the hardness,  $H$ , and the reduced Young's modulus,  $E^*$ , can be calculated. The evolution of hardness and reduced Young's modulus were obtained vs the penetration depth.

The indentation load  $F$  was applied exponentially as a function of time, and the ratio  $F'/F$  was  $0.03 \text{ s}^{-1}$ , where  $F'$  is the derivative of the indentation force with respect to time. The maximal indentation load was 450 mN. Meanwhile, the Loubet model was used to calculate the contact area, which takes into account piling-up or sinking-in of material during measurement [24]. The measurement was repeated nine times at different positions on each sample. The results presented a good repeatability and Fig. 4 shows the mean values.

For the Ti-6Al-4V substrate, the hardness  $H$  is  $3.4 \pm 0.5$  GPa, and the reduced Young's modulus  $E^*$  is around  $120 \pm 14$  GPa. Furthermore, with the increase in the penetration depth, the hardness shows a slight decrease at low penetration depth ( $< 500$  nm), probably due to the tip defect [26].

For the DLC coated flat, the hardness and reduced Young's modulus are larger than those for the substrate. The evolution of hardness with the penetration depth presents a short plateau between 50 and 200 nm, with an average hardness of  $29 \pm 4.5$  GPa. After that, the hardness drastically decreases because of the "substrate effect". For the Young's modulus, no plateau is observed. The average value of reduced Young's modulus is around  $240 \pm 24$  GPa between 50 and 150 nm and 150 nm.

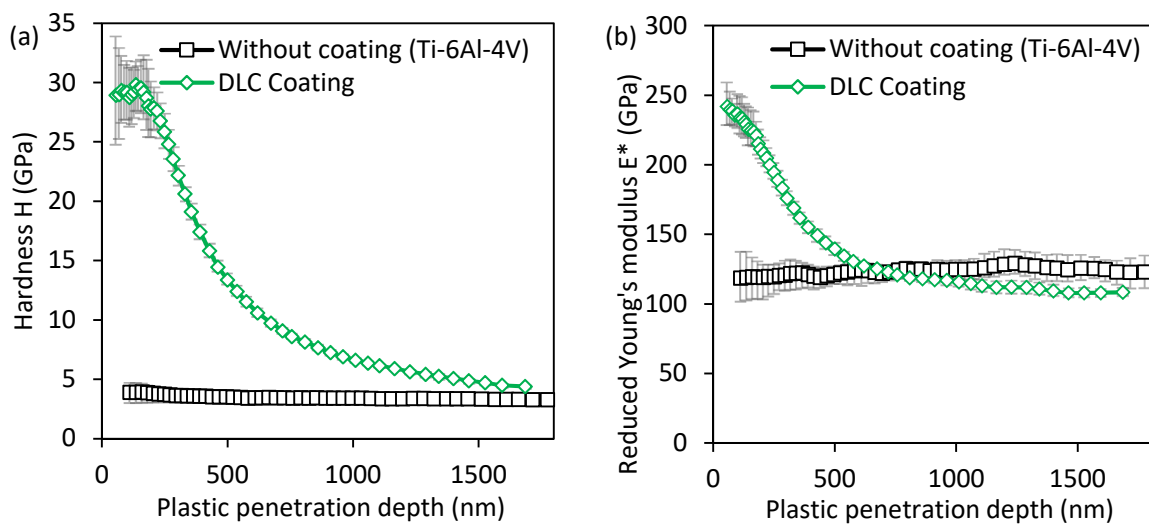


Fig. 4. (a) Nano-hardness and (b) reduced Young's modulus of the DLC coated smooth flat and the Ti-6Al-4V substrate.

## 2.2. Evolution of friction coefficient during fretting experiments

The friction coefficient  $\mu$  is defined as the maximal tangential force  $Q_{\max}$  divided by the normal force  $P$  applied during a fretting force/displacement cycle. The evolution of the friction coefficient and the fretting log are shown in Fig. 5. The fretting is in the gross slip regime (Fig. 5b). The friction coefficient  $\mu$  shows an increase during the first 10 cycles, which are called the ramping-in period, i.e., the displacement amplitude of the test rig increased gradually during the first 10 cycles and then reached the set value ( $\pm 20$   $\mu\text{m}$  in this study). After that, the friction coefficient decreases rapidly from around 0.75 to a lower value (around 0.25) during the first 100 cycles (i.e., the running-in period), then it remains low and relatively steady until the end of the test.

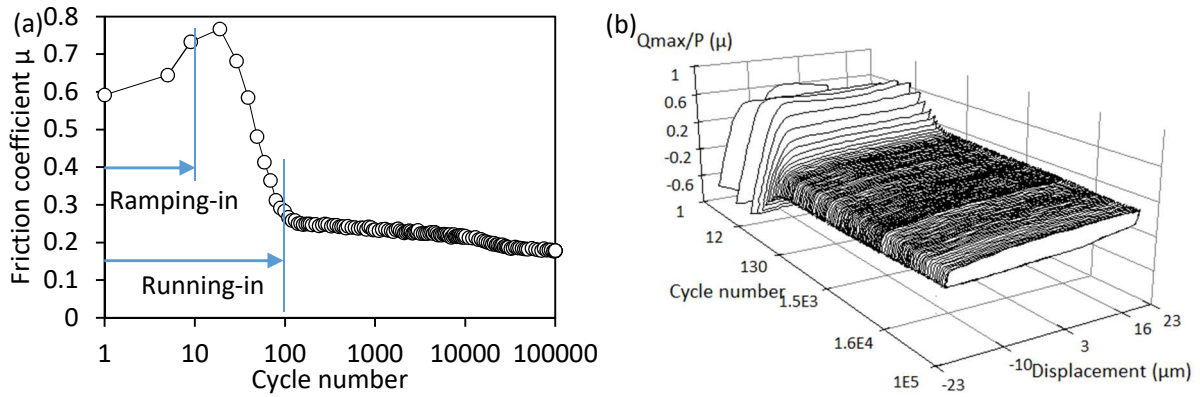


Fig. 5. (a) Evolution of friction coefficient and (b) fretting log.

### 2.3. DLC coating surface after fretting

Fig. 6 shows the DLC coating surface after the fretting test. In the wear scar, scratches were generated parallel to the sliding direction. Neither obvious perforation nor delamination of coating was observed in this study. However, according to our previous works [19], the DLC coating could be broken and delaminated under larger forces. Furthermore, surface roughness had influence on the tribological performance of the DLC coating. A rougher surface could cause more severe damage of coating [19].

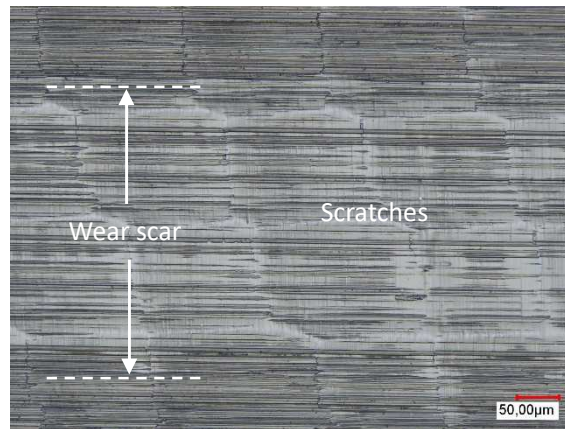


Fig. 6. DLC coating surface after fretting test.

### 2.4. Tribofilm characterization

Fig. 7 shows the tribofilm formed on the Ti-6Al-4V flat surface after the fretting test. It is clear that the Ti-6Al-4V was worn off, resulting in scratches on the surface (Fig. 7b). Meanwhile, some worn-off material was trapped and pressed in the contact, forming a tribofilm (Figs. 7a,b). From the EDX analysis (Fig. 7d), the tribofilm was composed of titanium (around 60 wt%), aluminum, vanadium, and a quantity of oxygen (around 30 wt%), suggesting that the tribofilm was mainly composed of the oxidized wear product of Ti-6Al-4V alloy. Furthermore, cracks were generated perpendicularly to the sliding direction

probably due to the repeated sliding and the stress variation (Fig. 7c).

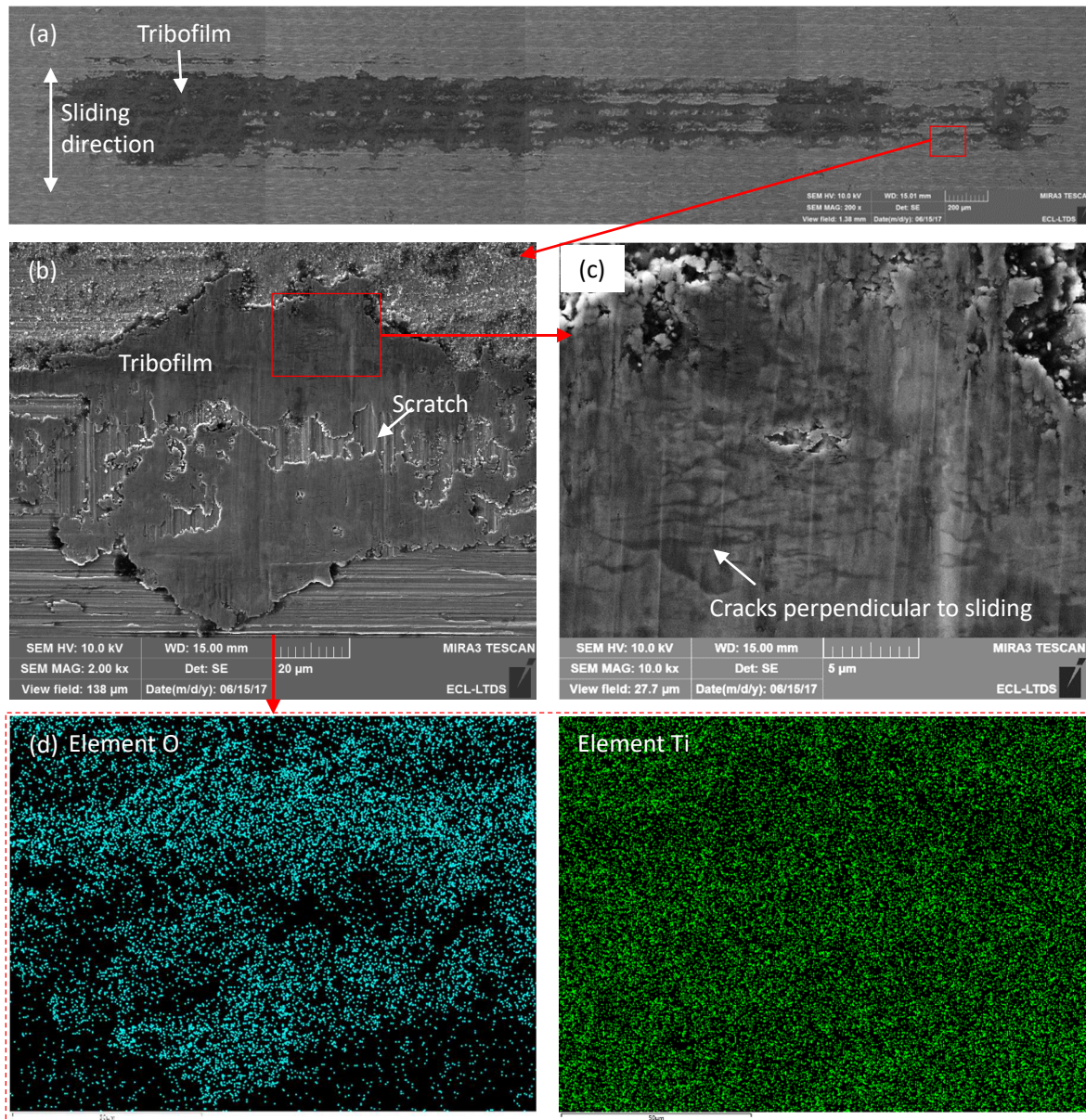


Fig. 7. Tribofilm formed on Ti-6Al-4V flat surface: (a) global view; (b) zoom of figure (a); (c) zoom of figure (b); (d) EDX analysis of figure (b).

The cross section of the Ti-6Al-4V flat is shown in Fig. 8. In the center area of the contact, the tribofilm thickness reaches around  $0.7 \mu\text{m}$  (Fig. 8a). The tribofilm material heaps up in the valley on the border area of the contact, leading to the thickness of approximately  $2 \mu\text{m}$  (Fig. 8b).

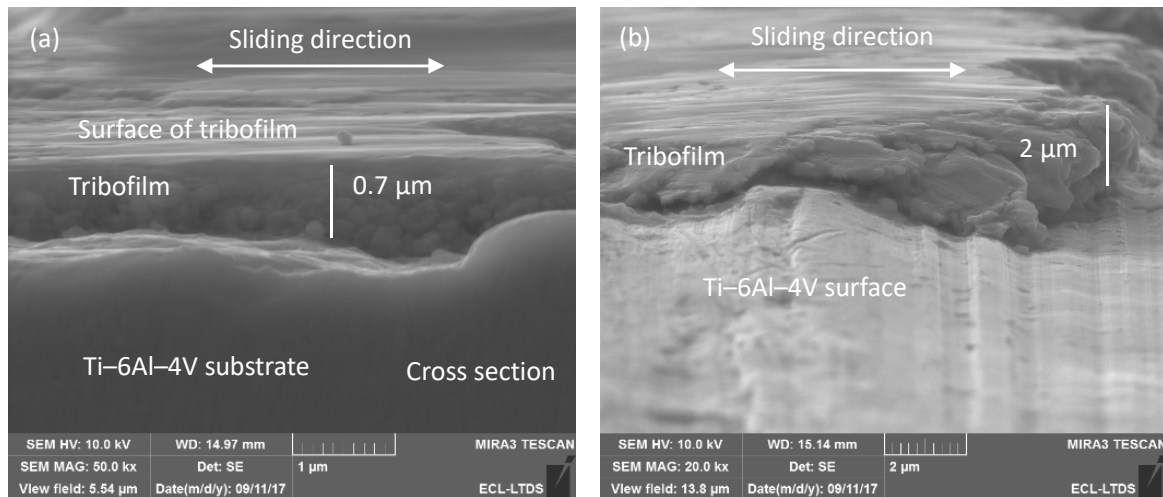


Fig. 8. Cross section of Ti-6Al-4V flat: (a) center area and (b) border area of the contact.

In summary, when the Ti-6Al-4V alloy slid against the DLC coating under ambient atmosphere, the friction coefficient decreased rapidly from around 0.75 to low values (around 0.25) in the running-in period of around 100 cycles. A tribofilm (with the thickness of around 0.7–2 μm) was formed on the rubbed Ti-6Al-4V surface. The tribofilm was mainly composed of severe oxidized wear product of Ti-6Al-4V alloy. **In addition, the rubbed DLC surface and the tribofilm surface were analyzed via Raman spectroscopy in previous works [20]. Structural transformation occurred on the rubbed DLC surface, and the transformed material was transferred onto the tribofilm surface, forming a carbonaceous layer. Meanwhile, according to the EDX observation of the tribofilm, the darker the area (for example the filling material in the crack), the more carbon element was detected [20]. This was consistent with the results from Raman spectroscopy. It should be noted that the countersurface (i.e. the DLC coating) played an important role in the generation of tribofilm and the low friction. When the Ti-6Al-4V flat slid against an untreated Ti-6Al-4V cylinder, no tribofilm was formed on the Ti-6Al-4V surface, and the friction was high in the range of 1.0-1.2 [19,20]. In the following two sections, the mechanical properties of the tribofilm and the Ti-6Al-4V substrate will be characterized using nano-indentation and micro-pillar compression tests.**

### 3. Nano-indentation on tribofilm and Ti-6Al-4V substrate

Nano-indentation tests were performed on tribofilm and Ti-6Al-4V substrate to measure their mechanical properties. The maximal indentation load was 100 mN. The indentation test was repeated nine times at different positions. Fig. 9 shows representative imprints and Fig. 10 shows the means values of nano-hardness and reduced Young's modulus **from nine indentation tests. The error bars represent the standard deviation of results from the nine tests.**

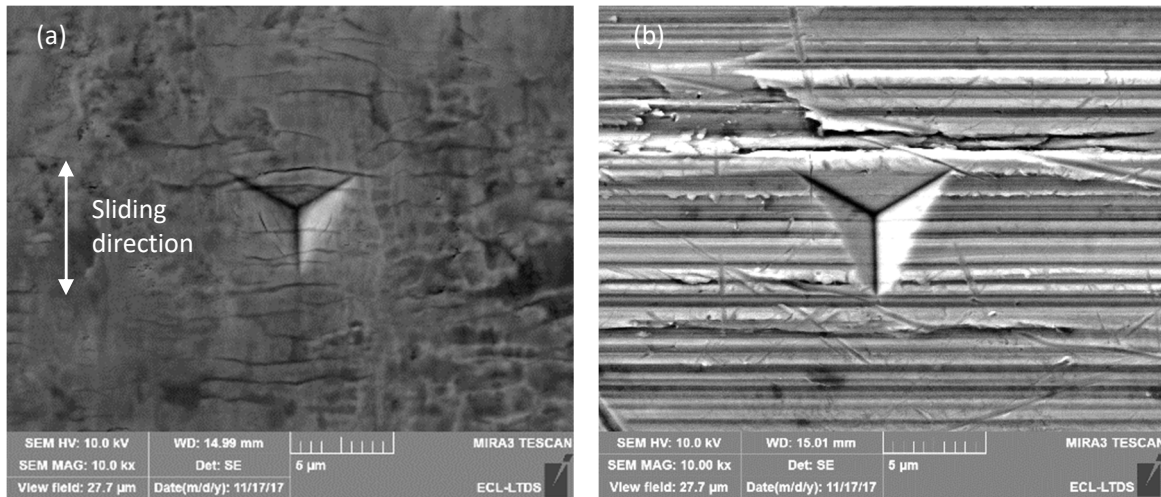


Fig. 9. Residual imprints after nano-indentation: (a) on tribofilm; (b) on Ti-6Al-4V substrate.

For the Ti-6Al-4V substrate, with the increase in the penetration depth, the hardness shows a slight decrease at low penetration depth ( $< 200$  nm), probably due to the “indentation size effect” and/or the tip defect [26]. The average value of hardness  $H$  over the penetration depth is  $3.9 \pm 1.5$  GPa ( $\pm$  represents the standard deviation of the values of dots on the curve in Fig. 10a), and the reduced Young’s modulus  $E^*$  is  $130 \pm 30$  GPa. Comparing with the results obtained on the smooth Ti-6Al-4V flat (Fig. 4), the values obtained on the rough Ti-6Al-4V flat present a larger deviation especially at the small penetration depths (Fig. 10), which is because of the high surface roughness (Fig. 9b).

For the tribofilm, the hardness is higher than that of the substrate. With increasing the penetration depth, there is a plateau between  $50$  and  $160$  nm, with an average value of  $10 \pm 0.4$  GPa, which is approximately 2.6 times higher than the hardness of the Ti-6Al-4V substrate. After that, the hardness decreases due to the “substrate effect”. Concerning the reduced Young’s modulus, the average value between  $60$  and  $120$  nm is  $170 \pm 3$  GPa, which is 1.3 times higher than the reduced Young’s modulus of the Ti-6Al-4V substrate.

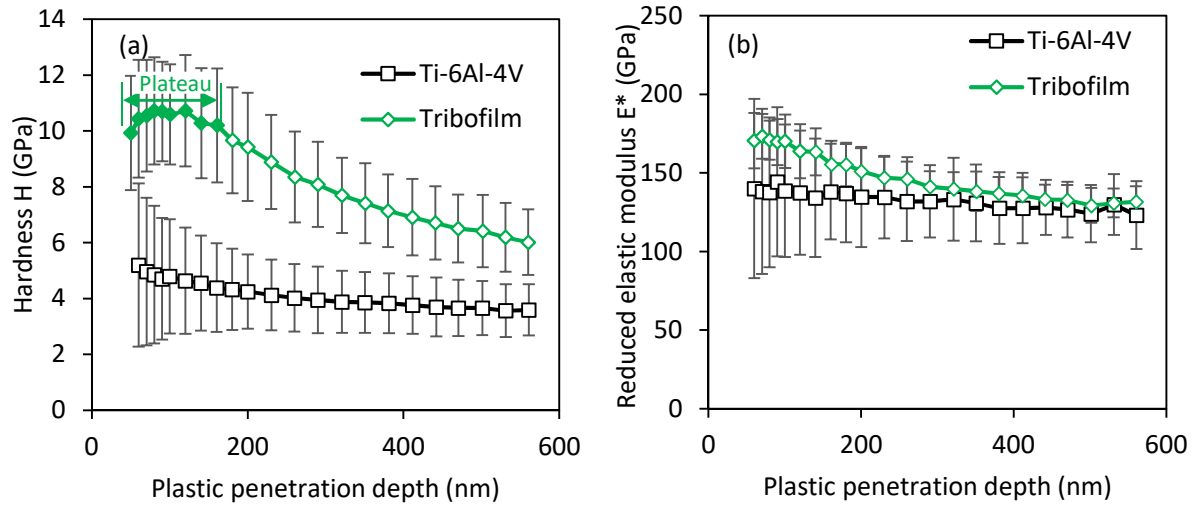


Fig. 10. (a) Nano-hardness and (b) reduced Young's modulus of tribofilm and Ti-6Al-4V substrate.

#### 4. Micro-pillar compression on tribofilm and Ti-6Al-4V substrate

##### 4.1. Preparation of micro-pillar

Micro-pillars were made in the tribofilm and Ti-6Al-4V surface using the FIB. They were machined using a gallium ion source in FEI Helios NanoLab™ DualBeam™ microscope. Several steps were conducted: from 21 nA to 80 pA at 30 kV to obtain clean and homogeneous pillar surfaces.

Two micro-pillar geometries were achieved (shown in Fig. 11): (1) small pillars: diameter  $\approx 1.3 \mu\text{m}$ , height  $\approx 2.0 \mu\text{m}$ , and tapering angle  $\approx 4^\circ$ ; and (2) large pillars: diameter  $\approx 4.0 \mu\text{m}$ , height  $\approx 7.0 \mu\text{m}$ , and tapering angle  $\approx 4^\circ$ . On the Ti-6Al-4V surface, both small and large pillars were milled. On the tribofilm, because of its small thickness, only small pillars were milled. In total, three large pillars on Ti-6Al-4V (numbered as #1, #2, #3, respectively), three small pillars on Ti-6Al-4V (numbered as #4, #5, #6, respectively), and six small pillars on tribofilm (numbered as #7, #8, #9, #10, #11, #12, respectively) were adopted for compression testing.

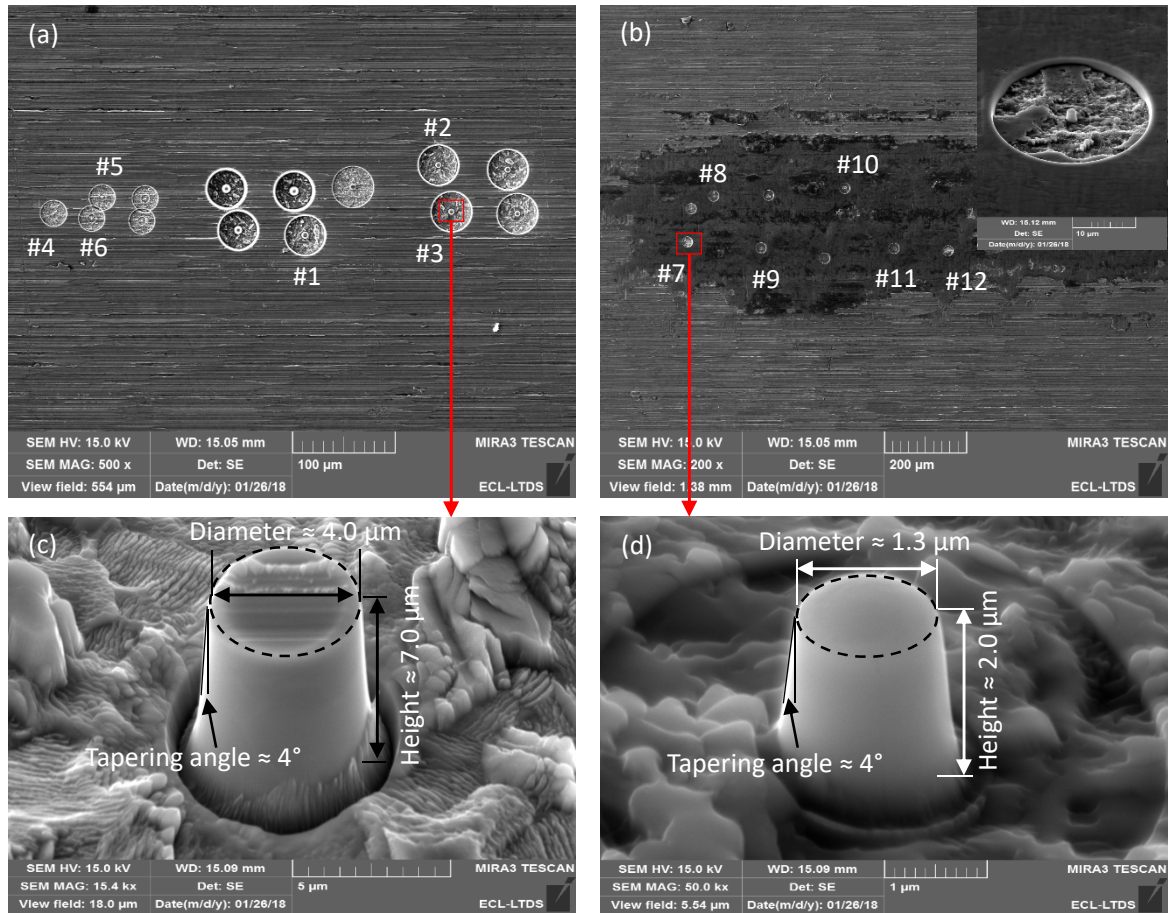


Fig. 11. (a) Pillars on Ti-6Al-4V; (b) pillars on tribofilm; (c) larger pillar on Ti-6Al-4V; (d) smaller pillar on tribofilm.

#### 4.2. Stress–strain curves of micro-pillar compression

Micro-pillars were compressed using a standard Alemnis SEM indenter [22]. The micro-compression tests were performed inside the SEM using a 10  $\mu\text{m}$  diameter diamond flat punch. The speed of the indenter was 0.014  $\mu\text{m/s}$ . During compression, the compression force and the displacement were recorded. The displacement of the pillar was corrected from thermal drift, sample and punch compliance based on Sneddon’s relationship [24,36], and frame compliance. Thus, the force–displacement ( $F-\delta$ ) curves were obtained. Then, the stress was calculated by dividing the measured load by the pillar upper surface area before compression. The strain was calculated by dividing the displacement by the pillar height before compression [30]. Thus, the stress–strain ( $\sigma-\varepsilon$ ) curves were obtained.

Fig. 12 shows the stress–strain curves for all the pillars. It is clear that the pillars on tribofilm present higher yield strength than the pillars on Ti-6Al-4V. The compression behaviors of large Ti-6Al-4V pillars, small Ti-6Al-4V pillars, and small pillars on tribofilm will be discussed in detail, respectively.

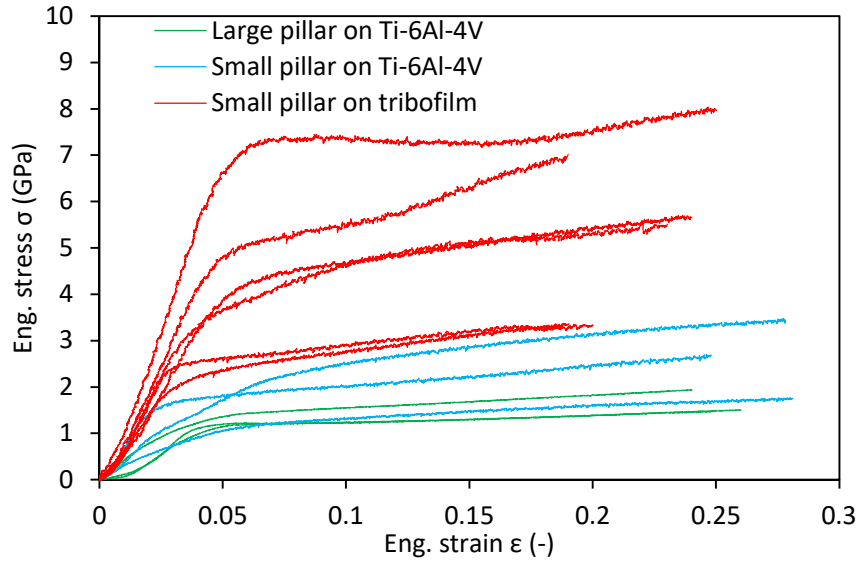


Fig. 12. Stress–strain ( $\sigma$ – $\epsilon$ ) curves for micro-pillar compression.

#### 4.2.1. Large Ti–6Al–4V pillar

Fig. 13 shows the stress–strain curve for a representative large Ti–Al–4V pillar (#3). The corresponding SEM images are shown in Fig. 14.

According to the stress–strain curve, the micro-compression underwent four domains. In domain (1), the asperities of the rough Ti–6Al–4V surface firstly came into contact with the punch. The contact was asperities-on-punch contact. The asperities had low stiffness, leading to a small slope of stress to strain (i.e.,  $\Delta\sigma/\Delta\epsilon$  ratio). With compression force increasing, the asperities were pressed and the true contact area increased, thus the  $\Delta\sigma/\Delta\epsilon$  ratio increases gradually. In domain (2), the stress–strain curve is linear-like. The pillar underwent elastic deformation. In domain (3), the pillar underwent elasto-plastic deformation and cracks started to generate and propagate (as shown in Fig. 14d). The slope of stress to strain ( $\Delta\sigma/\Delta\epsilon$  ratio) decreases gradually. In domain (4), severe plastic deformation occurred. More cracks were generated and the pillar deformed via double slip (Fig. 14e). Significant slip at the crack interface resulted in a much lower  $\Delta\sigma/\Delta\epsilon$  ratio. The pillar shape became barrel-like.

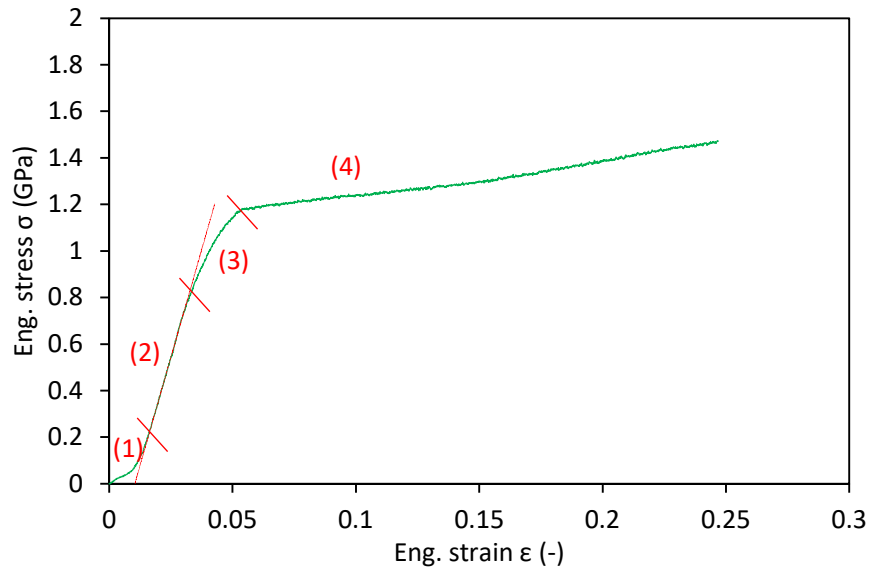


Fig. 13. Representative stress–strain curve for a large Ti–6Al–4V pillar.

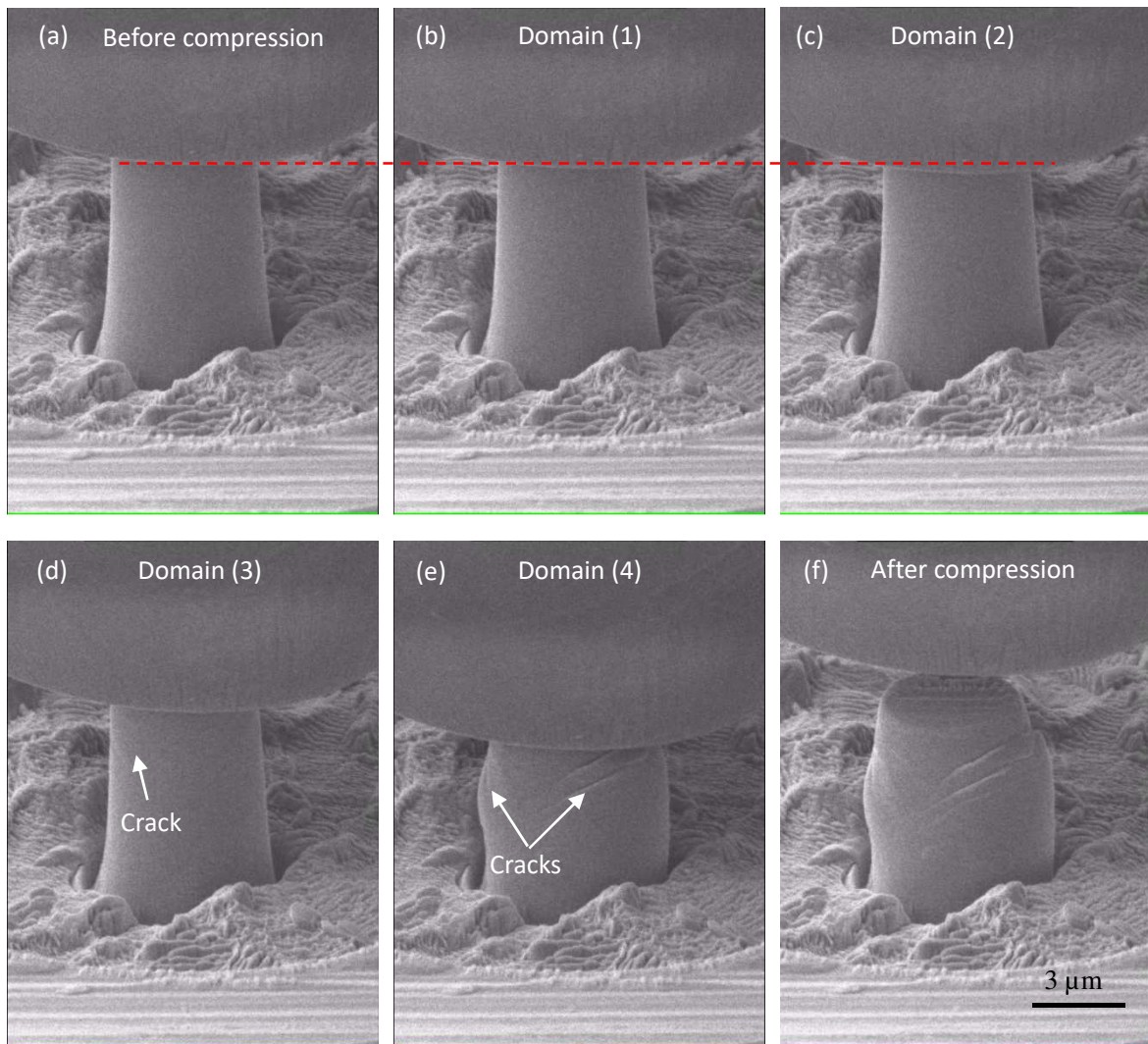


Fig. 14. SEM observation of compression on a large Ti–6Al–4V pillar: (a) before compression; (b) in domain (1); (c) in domain (2); (d) in domain (3); (e) in domain (4); and (f) after compression.

#### 4.2.2. Small Ti–6Al–4V pillar

Fig. 15 shows stress–strain curves for small Ti–6Al–4V pillars. Fig. 16 shows SEM images of two pillars (#5 and #6) after compression.

It is clear that, for small Ti–6Al–4V pillars, the domain (1) of stress–strain curves is significantly shorter comparing with that for large Ti–6Al–4V pillars, because the effect of original surface roughness (i.e., asperities) was weaker on small pillars. Besides, these three curves show obvious difference to each other (including different  $\Delta\sigma/\Delta\varepsilon$  ratios in domain (2), and different stresses in domain (4)). This is because the studied Ti–6Al–4V is  $\alpha$ – $\beta$  alloy, which is composed of  $\alpha$  phases and  $\alpha + \beta$  phases. The  $\alpha + \beta$  phases have a lamellar structure. The anisotropic structure led to a stochastic mechanical response throughout the deformation, which became increasingly evident for smaller pillars. From SEM images of compressed pillars, cracks generated and severe plastic deformation occurred. The compressed pillar #5 was barrel-like (Fig. 16a); and the pillar #6 was deformed relatively homogeneously (Fig. 16b).

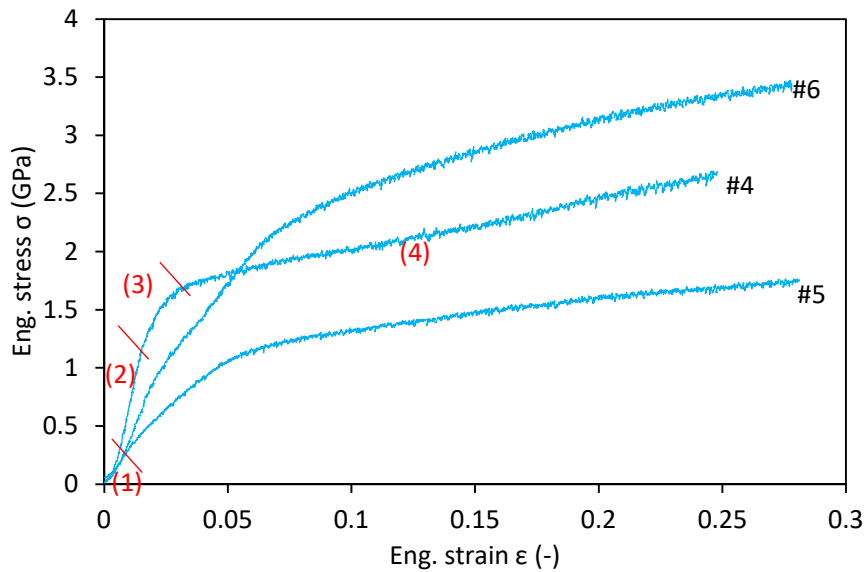


Fig. 15. Stress–strain curves for small Ti–6Al–4V pillars.

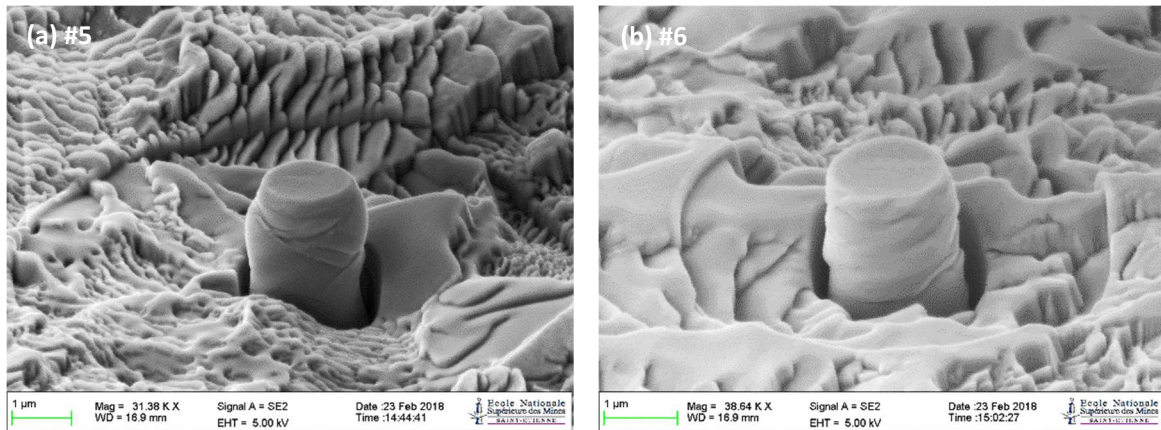


Fig. 16. SEM observation of small Ti-6Al-4V pillars after compression: (a) pillar #5; (b) pillar #6.

#### 4.2.3. Small pillar on tribofilm

Fig. 17 shows the stress–strain curves for small pillars on tribofilm. Fig. 18 shows SEM images of two pillars (#9 and #12) before and after compression. In addition, From Fig. 9a, cracks were generated in the tribofilm during fretting. However, the diameter of pillars was small and no obvious cracks were observed in the pillars (Figs. 18 a, c). Thus, the results of micro-compression could offer the representative mechanical properties of the pillar material.

It is clear that, for pillars on tribofilm, the domain (1) of stress–strain curves is further shorter than Ti-6Al-4V pillars, because of the smoothness of tribofilm surface.

It should be noted that the thickness of the tribofilm was not constant but in the range of around 0.7–2.0 µm. Micro-pillars were fabricated using FIB in the tribofilm with the height of around 2.0 µm. During FIB etching, the etched tribofilm and the etched Ti-6Al-4V substrate showed different topographies. The Ti-6Al-4V substrate showed a rough surface (as shown in Fig. 11a), while the tribofilm showed a smooth appearance (as shown in Fig. 17a). After FIB etching, if the bottom of the pool showed a smooth surface, the localized tribofilm thickness was larger than the pillar height. The corresponding pillar was only composed of tribofilm material. If the bottom of the pool showed a rough surface, the localized tribofilm thickness was smaller than the pillar height. The corresponding pillar was composed of tribofilm material in the upper part and the Ti-6Al-4V alloy in the bottom part.

For pillar #9, it was made on the tribofilm where the thickness was larger than the pillar height. The pillar was only composed of tribofilm material. The stress–strain curve represents the mechanical property of the tribofilm material. The pillar has the highest stress in domain (4), as shown in Fig. 17. After compression, a crack was generated, but the plastic deformation was not discernible (Fig. 18b).

For other pillars (including #12), they were made on the tribofilm where the thickness

was smaller than the pillar height. Thus, these pillars were composed of the tribofilm material in the upper part and the Ti-6Al-4V alloy in the bottom part. The stress-strain curves represent the combined consequence of the upper tribofilm material and the bottom Ti-6Al-4V alloy. These pillars have relatively lower stresses than pillar #9 (Fig. 17), but higher stresses than the pure Ti-6Al-4V pillars (Fig. 12). Figs. 18c,d show a representation (#12) of this kind of pillars. After compression, in the upper part (i.e., the tribofilm), a crack was generated, but the plastic deformation was not discernible. In the bottom part (i.e., the Ti-6Al-4V alloy), severe plastic deformation occurred, and the shape became barrel-like.

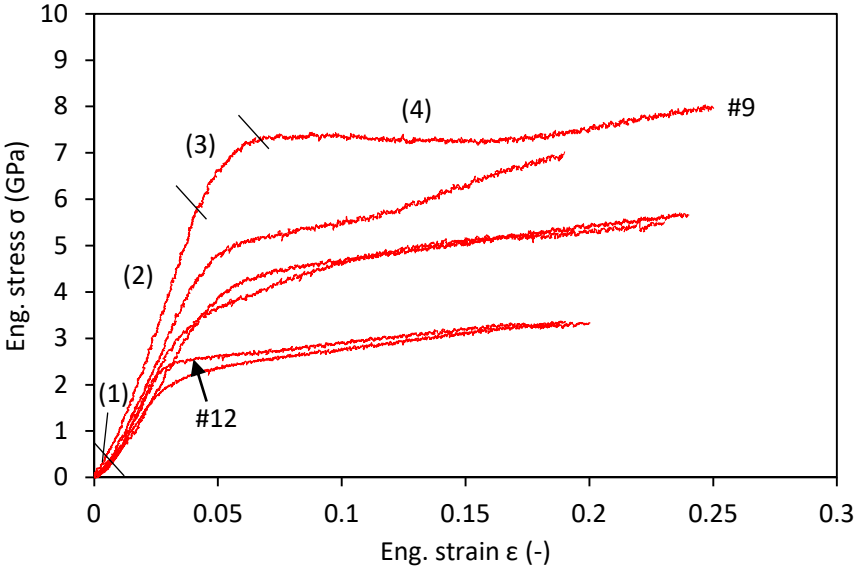
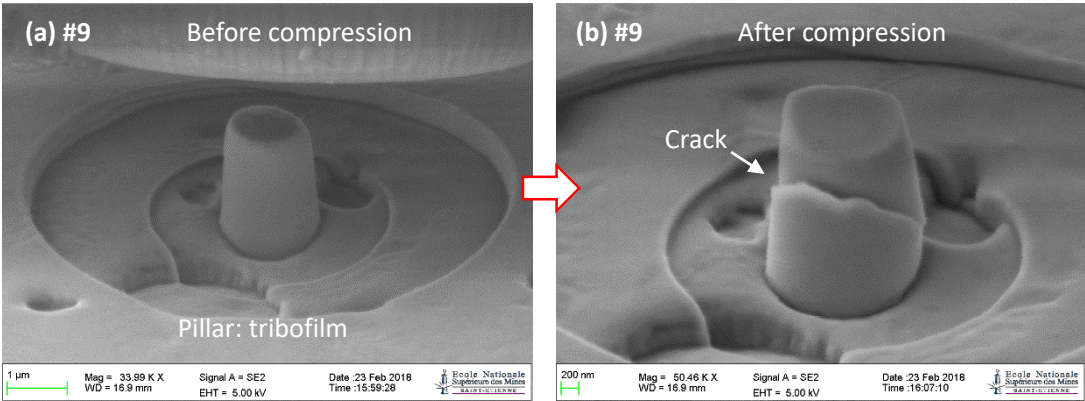


Fig. 17. Stress-strain curves for small pillars on tribofilm.



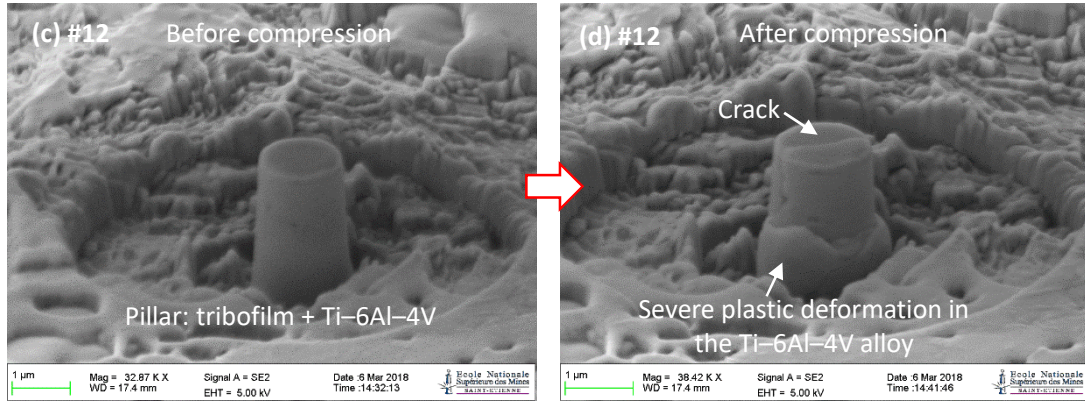


Fig. 18. SEM observation of small pillars on tribofilm before and after compression: (a) and (b) pillar #9; (c) and (d) pillar #12.

### 4.3. Compression modulus of micro-pillar

The compression modulus ( $E_s$ ) is not easy to obtain by micro-compression due to misalignment problems. In this study, the compression modulus is defined as the slope of stress to strain (i.e.,  $\Delta\sigma/\Delta\epsilon$  ratio) in the domain (2) (i.e., in the elastic deformation period), as shown in Fig. 19.

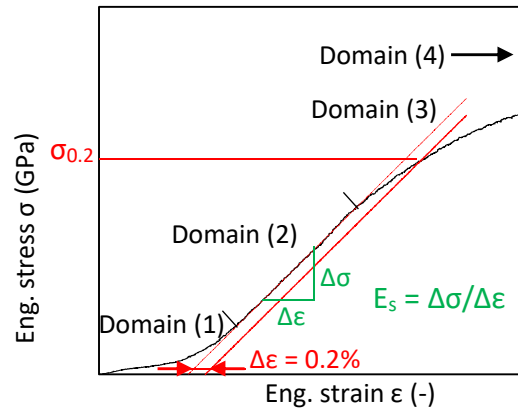


Fig. 19. Calculation processes of compression modulus ( $E_s$ ) and yield strength ( $\sigma_{0.2}$ ).

Fig. 20 shows all the compression moduli for pillars on Ti-Al-4V and tribofilm. For large Ti-6Al-4V pillars, the average value of compression moduli is approximately 47 GPa. For small Ti-6Al-4V pillars, the average value of compression moduli is approximately 62 GPa with a large deviation. For small pillars on the tribofilm, the average value of compression moduli is approximately 110 GPa, that is around two times larger than the Ti-6Al-4V pillars. Furthermore, the pure tribofilm pillar (#9) exhibits the highest compression modulus of around 160 GPa. The pillars, which consist of tribofilm material in the top part and Ti-6Al-4V alloy in the bottom part, exhibit relatively lower compression moduli than the pure tribofilm pillar (#9). It can be concluded that the compression modulus ( $E_s$ ) of tribofilm is significantly larger than that of Ti-6Al-4V substrate.

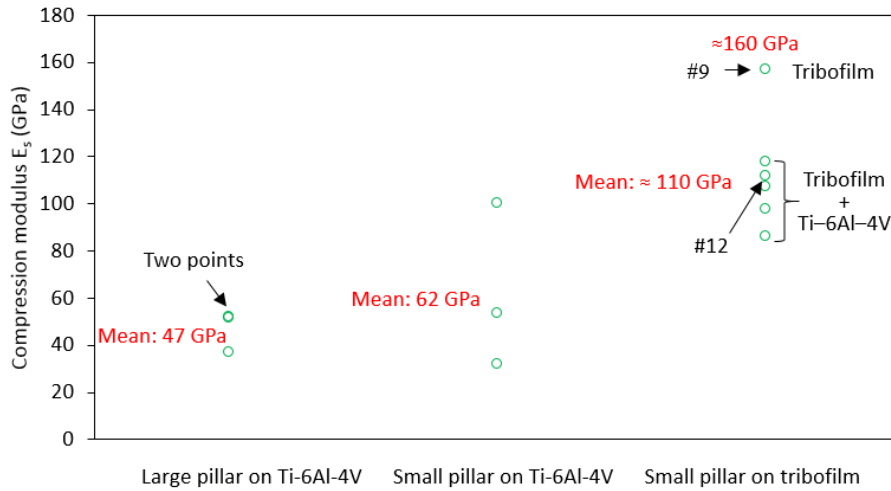


Fig. 20. Compression moduli of various micro-pillars.

#### 4.4. Yield strength of micro-pillar compression

The yield strength ( $\sigma_{0.2}$ ) is set as the stress ( $\sigma$ ) at 0.2% plastic strain. The effect of plastic deformation of asperities in domain (1) is removed, as shown in Fig. 19.

Fig. 21 shows all the values of yield strength ( $\sigma_{0.2}$ ) for pillars on Ti-6Al-4V and tribofilm. For large Ti-6Al-4V pillars, the average value of yield strength is approximately 0.90 GPa. For small Ti-6Al-4V pillars, the average value of yield strength ( $\sigma_{0.2}$ ) is approximately 0.95 GPa. For small pillars on the tribofilm, the average value of yield strength is approximately 3.6 GPa, that is around four times larger than the Ti-6Al-4V pillars. Furthermore, the pure tribofilm pillar (#9) exhibits the highest yield strength of around 6.4 GPa. The pillars, which consist of tribofilm material in the top part and Ti-6Al-4V alloy in the bottom part, exhibit relatively lower yield strength than the pure tribofilm pillar, but higher than the pure Ti-6Al-4V pillars. It can be concluded that, in the micro-pillar compression test, the yield strength ( $\sigma_{0.2}$ ) of tribofilm is significantly larger than that of Ti-6Al-4V substrate.

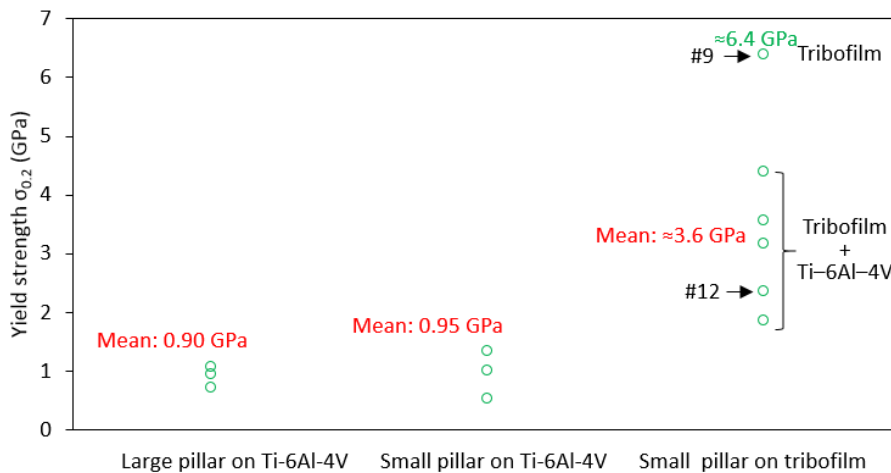


Fig. 21. Yield strength of micro-pillars compression.

## 5. Discussion

### 5.1. Nano-indentation vs. micro-compression

The mechanical properties of the tribofilm and Ti-6Al-4V were measured using both nano-indentation and micro-pillar compression techniques, as shown in Table 1. Through nano-indentation tests, hardness (H) and reduced Young's modulus ( $E^*$ ) were obtained. Through micro-pillar compression tests, compression modulus ( $E_s$ ) and yield strength ( $\sigma_{0.2}$ ) were obtained. The results from nano-indentation and micro-pillar compression techniques can be compared.

According to the experimental Tabor relationship for metals [37], in which the hardness and yield strength are commonly correlated as  $H/\sigma_{0.2} \approx 3$  [30], the hardness (H) can be deduced from compression tests (i.e., from the yield strength). For Ti-6Al-4V alloy, the deduced hardness from compression test is in the range of around 2.7–2.9 GPa (Table 1). The hardness from nano-indentation test is around  $3.9 \pm 1.5$  GPa (when the maximal indentation load was 100 mN, Table 1) and around  $3.4 \pm 0.5$  GPa (when the maximal indentation load was 450 mN, Fig. 4a). The values of hardness from both nano-indentation and micro-pillar compression techniques show rather similar values. For tribofilm, the deduced hardness of pure tribofilm pillar (#9) is around 19 GPa (Table 1). The hardness from nano-indentation test is around  $10 \pm 0.4$  GPa. The hardness obtained from nano-indentation test is almost a half of that from micro-pillar compression test. Furthermore, the average value of yield strength from all the pillars on tribofilm (both pure tribofilm pillar and pillars with Ti-6Al-4V at the bottom part) is around 3.6 GPa (Fig. 21). The deduced hardness is around 11 GPa, that is very close to the hardness from nano-indentation test ( $10 \pm 0.4$  GPa). This indicates that the hardness of tribofilm obtained from nano-indentation is lower than the true hardness of the tribofilm, which is probably due to the “substrate effect” of nano-indentation even at a relatively low penetration depth.

Table 1. Mechanical properties of the tribofilm and Ti-6Al-4V. For nano-indentation on tribofilm, values of hardness H and reduced Young's modulus were adopted at low penetration depth. For micro-compression on tribofilm, the results of pillar #9 (pure tribofilm pillar) were adopted. Hardness H from micro-compression was deduced from yield strength  $\sigma_{0.2}$  with the relationship  $H/\sigma_{0.2} \approx 3$ .

Techniques	Mechanical properties	Ti-6Al-4V	Tribofilm	Ratio of tribofilm to Ti-6Al-4V
Nano-indentation	Hardness H (GPa)	$3.9^{\pm 1.5}$	$10^{\pm 0.4}$	2.6
	Reduced Young's modulus $E^*$ (GPa)	$130^{\pm 30}$	$170^{\pm 3}$	1.3
	Compression modulus $E_s$ (GPa)	47–62	160	2.5–3.3

Micro-pillar compression	Yield strength $\sigma_{0.2}$ (GPa)	0.90–0.95	6.4	6.7–7.1
	Hardness H (GPa)	$\approx 2.7$ – $2.9$	$\approx 19$	6.7–7.1

In addition, the compression modulus from micro-pillar compression is significantly lower than the reduced Young's modulus (as well as the Young's modulus) from nano-indentation, especially on the Ti–6Al–4V alloy. This difference on elasticity from both techniques was also observed in previous works on pure iron [31]. This is because these two techniques exam different aspects of elastic properties. For the micro-pillar compression, the uniaxial nature of the loading tests for the weakest link of the pillar, while, the nano-indentation probes a small volume around the indentation.

In summary, when measuring the hardness on the Ti–6Al–4V bulk, both the nano-indentation and micro-pillar compression tests exhibited similar results. However, when measuring the hardness on the tribofilm, **nano-indentation test presented lower values than micro-pillar compression test, which was probably due to the “substrate effect” of nano-indentation.** Besides, the micro-pillar compression could offer another aspect of elastic property—compression modulus ( $E_s$ )—in addition to the reduced Young's modulus from nano-indentation. Furthermore, the micro-pillar compression led to the measurement of the stress–strain behavior and allowed to see directly the deformation of the pillar using a SEM for better understanding of deformation mechanism.

**In addition, as mentioned in the introduction part, pillars were fabricated using a FIB which might induce a thermally affected zone at the pillar edge, and this thermal effect might cause the change in the mechanical properties of the pillar. In the present study, there was no direct evidence of this change in the mechanical properties caused by pillar fabrication.**

## 5.2. Tribofilm vs. Ti–6Al–4V

The mechanical properties of the tribofilm and Ti–6Al–4V alloy are compared, as shown in Table 1. It is clear that the tribofilm is harder and stiffer than the Ti–6Al–4V alloy. Specifically, from nano-indentation tests, the hardness (H) of tribofilm ( $10 \pm 0.4$  GPa) is 2.6 times higher than that of Ti–6Al–4V alloy ( $3.9 \pm 1.5$  GPa). The reduced Young's modulus ( $E^*$ ) of tribofilm ( $170 \pm 3$  GPa) is around 1.3 times higher than that of Ti–6Al–4V alloy ( $130 \pm 30$  GPa). From micro-pillar compression tests, the compression modulus ( $E_s$ ) of tribofilm (around **160** GPa) is 2.5–3.3 times higher than that of Ti–6Al–4V alloy (47–62 GPa). The yield strength ( $\sigma_{0.2}$ ) of tribofilm (around **6.4** GPa) is 6.7–7.1 times higher than that of Ti–6Al–4V alloy (0.90–0.95 GPa). Consequently, the deduced hardness (H) from the yield strength of tribofilm (around **19** GPa) is also 6.7–7.1 times higher than that of Ti–6Al–4V alloy (around

2.7–2.9 GPa).

The increase in **hardness and elasticity** of tribofilm was probably related to the refined structure. The tribofilm was derived from wear product of Ti–6Al–4V alloy and underwent repeated **severe** deformation action, which might lead to grain refinement. This can be verified to some extent from the observation of the FIB made surfaces. The etched Ti–6Al–4V substrate shows a rough surface with lamellar microstructure (Fig. 16). While, the etched tribofilm surface exhibits an extremely smooth surface (Fig. 18a), which could suggest a fine structure. Furthermore, the repeated deformation action of the tribofilm material might lead to an increase in dislocation densities, which could also **improve the hardness**. In addition, the oxidization of the tribofilm might also contribute to the improved **hardness**. It is widely observed in previous works [38,39] that the titanium oxide layers presented increased **hardness values**.

The hardness of tribofilm has an influence on the friction response. Specifically, we can consider that the friction force  $F$  can be calculated as:

$$F = AY \quad (1)$$

where  $A$  is the contact area, and  $Y$  is the shear stress. The true contact area  $A$  is

$$A = W/H \quad (2)$$

where  $W$  is the normal load, and  $H$  is the hardness of the softer material of the friction pair [4]. In this study, the hardness of tribofilm ( $10 \pm 0.4$  GPa from nano-indentation, around **19** GPa deduced from micro-pillar compression) is lower than the DLC coating ( $29 \pm 4.5$  GPa from nano-indentation, Fig. 3a). Thus, the  $H$  is the hardness of tribofilm. Therefore, the friction coefficient  $\mu$  can be calculated as:

$$\mu = F/W = Y/H \quad (3)$$

**From our previous works [20], structural transformation occurred on the rubbed DLC coating surface. The transformed carbonaceous material was also transferred to the tribofilm surface, forming a carbonaceous layer. We could make an assumption that shearing mainly occurred at the interface of tribofilm / DLC coating. The carbonaceous material between the DLC coating and the tribofilm could serve as a lubricant, which determined the shear stress  $Y$ .** In the present study, the hardness of the tribofilm was larger than the Ti–6Al–4V. The increased hardness of tribofilm also contributed to the decrease in the friction coefficient  $\mu$ .

## 6. Conclusions

Fretting tests were carried out with a Ti–6Al–4V / DLC coating contact under the ambient atmosphere. The friction coefficient  $\mu$  decreased from around 0.75 to around 0.25

during the running-in period of 100 cycles. A tribofilm was formed on the rubbed Ti-6Al-4V surface. The tribofilm was mainly composed of oxidized wear product of Ti-6Al-4V alloy. The thickness of the tribofilm was in the range of around 0.7–2.0  $\mu\text{m}$ .

The mechanical properties of the tribofilm and the Ti-6Al-4V alloy were characterized using nano-indentation and micro-pillar compression techniques. The tribofilm was harder and stiffer than the Ti-6Al-4V alloy. From nano-indentation tests, the hardness (H) of tribofilm ( $10 \pm 0.4$  GPa) was 2.6 times higher than that of Ti-6Al-4V alloy ( $3.9 \pm 1.5$  GPa). The reduced Young's modulus ( $E^*$ ) of tribofilm ( $170 \pm 3$  GPa) was around 1.3 times higher than that of Ti-6Al-4V alloy ( $130 \pm 30$  GPa). From micro-pillar compression tests, the compression modulus ( $E_s$ ) of tribofilm (around 160 GPa) was 2.5–3.3 times higher than that of Ti-6Al-4V alloy (47–62 GPa). The yield strength ( $\sigma_{0.2}$ ) of tribofilm (around 6.4 GPa) was 6.7–7.1 times higher than that of Ti-6Al-4V alloy (0.90–0.95 GPa).

When measuring the hardness on the Ti-6Al-4V bulk, both the nano-indentation and micro-pillar compression tests exhibited similar results. However, when measuring the hardness on the tribofilm, micro-pillar compression tests could obtain more accurate values than the nano-indentation tests.

### **Acknowledgements**

This work was supported by the LABEX MANUTECH-SISE (ANR-10-LABX-0075) of Université de Lyon, within the program "Investissements d'Avenir" (ANR-11-IDEX-0007) operated by the French National Research Agency (ANR). The authors would like to thank the China Scholarship Council for its financial support.

### **References**

- [1] R. Hauert, An overview on the tribological behavior of diamond-like carbon in technical and medical applications, *Tribology International* 37 (2004) 991–1003.
- [2] A. Grill, Diamond-like carbon: state of the art, *Diamond and Related Materials* 8 (1999) 428–434.
- [3] C.A. Love, R.B. Cook, T.J. Harvey, P.A. Dearnley, R.J.K. Wood, Diamond like carbon coatings for potential application in biological implants—a review, *Tribology International* 63 (2013) 141–150.
- [4] J. Robertson, Diamond-like amorphous carbon, *Materials Science and Engineering R* 37 (2002) 129–281.
- [5] K.D. Koshigan, F. Mangolini, J.B. McClimon, B. Vacher, S. Bec, R.W. Carpick, J. Fontaine, Understanding the hydrogen and oxygen gas pressure dependence of the

tribological properties of silicon oxide-doped hydrogenated amorphous carbon coatings, *Carbon* 93 (2015) 851–860.

[6] A. Grill, Review of the tribology of diamond-like carbon, *Wear* 168 (1993) 143–153.

[7] T. Kunze, M. Posselt, S. Gemming, G. Seifert, A.R. Konicek, R.W. Carpick, L. Pastewka, M. Moseler, Wear, plasticity, and rehybridization in tetrahedral amorphous carbon, *Tribology Letters* 53 (2014) 119–126.

[8] Y. Liu, A. Erdemir, E.I. Meletis, A study of the wear mechanism of diamond-like carbon films, *Surface and Coatings Technology* 82 (1996) 48–56.

[9] C. Donnet, J. Fontaine, A. Grill, T. Le Mogne, The role of hydrogen on the friction mechanism of diamond-like carbon films, *Tribology Letters* 9 (2000) 137–142.

[10] A.R. Konicek, D.S. Grierson, P.U.P.A. Gilbert, W.G. Sawyer, A.V. Sumant, R.W. Carpick, Origin of ultralow friction and wear in ultrananocrystalline diamond, *Physical Review Letters* 100 (2008) 235502.

[11] J-P. Hirvonen, R. Lappalainen, J. Koskinen, A. Anttila, T.R. Jervis, M. Trkula, Tribological characteristics of diamond-like films deposited with an arc-discharge method, *Journal of Materials Research* 5 (1990) 2524–2530.

[12] H. Ronkainen, J. Koskinen, J. Likonen, S. Varjus, J. Vihersalo, Characterization of wear surfaces in dry sliding of steel and alumina on hydrogenated and hydrogen-free carbon films, *Diamond and Related Materials* 3 (1994) 1329–1336.

[13] H. Erdemir, C. Donnet, Tribology of diamond-like carbon films: recent progress and future prospects, *Journal of Physics D: Applied Physics* 39 (2006) R311–R327.

[14] S. Fouvry, P. Duó, Ph. Perruchaut, A quantitative approach of Ti–6Al–4V fretting damage: friction, wear and crack nucleation, *Wear* 257 (2004) 916–929.

[15] B. van Peteghem, S. Fouvry, J. Petit, Effect of variable normal force and frequency on fretting wear response of Ti–6Al–4V contact, *Wear* 271 (2011) 1535–1542.

[16] M. Geetha, A.K. Singh, R. Asokamani, A.K. Gogia, Ti based biomaterials, the ultimate choice for orthopaedic implants – A review, *Progress in Materials Science* 54 (2009) 397–425.

[17] M.A.H. Gepreel, M. Niinomi, Biocompatibility of Ti-alloys for long-term implantation, *Journal of the Mechanical Behavior of Biomedical Materials* 20 (2013) 407–415.

[18] V. Fridrici, S. Fouvry, Ph. Kapsa, Effect of shot peening on the fretting wear of Ti–6Al–4V, *Wear* 250 (2001) 642–649.

[19] H.H. Ding, V. Fridrici, J. Geringer, J. Fontaine, Ph. Kapsa, Influence of diamond-like carbon coatings and roughness on fretting behaviors of Ti–6Al–4V for neck adapter–femoral stem contact, *Wear* 406–407 (2018) 53–67.

- [20] H.H. Ding, V. Fridrici, J. Geringer, J. Fontaine, Ph. Kapsa, Low-friction study between diamond-like carbon coating and Ti-6Al-4V under fretting conditions, *Tribology International* 135 (2019) 368–388.
- [21] C.C. Battaile, B.L. Boyce, C.R. Weinberger, S.V. Prasad, J.R. Michael, B.G. Clark, The hardness and strength of metal tribofilms: An apparent contradiction between nanoindentation and pillar compression, *Acta Materialia* 60 (2012) 1712–1720.
- [22] G. Guillonneau, M. Mieszala, J. Wehrs, J. Schwiedrzik, S. Grop, D. Frey, L. Philippe, J.-M. Breguet, J. Michler, J.M. Wheeler, Nanomechanical testing at high strain rates: New instrumentation for nanoindentation and microcompression, *Materials and Design* 148 (2018) 39–48.
- [23] R. Rabe, J.-M. Breguet, P. Schwaller, S. Stauss, F.-J. Haug, J. Patscheider, J. Michler, Observation of fracture and plastic deformation during indentation and scratching inside the scanning electron microscope, *Thin Solid Films* 469–470 (2004) 206–213.
- [24] G. Guillonneau, G. Kermouche, S. Bec, J.-L. Loubet, Extraction of mechanical properties with second harmonic detection for dynamic nanoindentation testing, *Experimental Mechanics* 52 (2012) 933–944.
- [25] J. Hay, P. Agee, E. Herbert, Continuous stiffness measurement during instrumented indentation testing, *Experimental Techniques* 34 (2010) 86–94.
- [26] J.G. Swadener, E.P. George, G.M. Pharr, The correlation of the indentation size effect measured with indenters of various shapes, *Journal of the Mechanics and Physics of Solids* 50 (2002) 681–694.
- [27] G. Dehm, H.P. Wörgötter, S. Cazottes, J.M. Purswani, D. Gall, C. Mitterer, D. Kiener, Can micro-compression testing provide stress–strain data for thin films? A comparative study using Cu, VN, TiN and W coatings, *Thin Solid Films* 518 (2009) 1517–1521.
- [28] D. Tumbajoy-Spinel, X. Maeder, G. Guillonneau, S. Sao-Joao, S. Descartes, J.-M. Bergheau, C. Langlade, J. Michler, G. Kermouche, Microstructural and micromechanical investigations of surface strengthening mechanisms induced by repeated impacts on pure iron, *Materials and Design* 147 (2018) 56–64.
- [29] J. Michler, K. Wasmer, S. Meier, F. Östlund, K. Leifer, Plastic deformation of gallium arsenide micropillars under uniaxial compression at room temperature, *Applied Physics Letters* 90 (2007) 043123.
- [30] A. Viat, G. Guillonneau, S. Fouvry, G. Kermouche, S. Sao-Joao, J. Wehrs, J. Michler, J.-F. Henne, Brittle to ductile transition of tribomaterial in relation to wear response at high temperatures, *Wear* 392–393 (2017) 60–68.

- [31] D. Tumbajoy-Spinel, S. Descartes, J.-M. Bergheau, V. Lacaille, G. Guillonnet, J. Michler, G. Kermouche, Assessment of mechanical property gradients after impact-based surface treatment: application to pure  $\alpha$ -iron, *Materials Science & Engineering A* 667 (2016) 189–198.
- [32] P. Stoyanov, D. Linsler, T. Schlarb, M. Scherge, R. Schwaiger, Dependence of tribofilm characteristics on the running-in behavior of aluminum–silicon alloys, *Journal of Materials Science* 50 (2015) 5524–5532.
- [33] S.Y. Jauch, G. Huber, H. Haschke, K. Sellenschloh, M.M. Morlock, Design parameters and the material coupling are decisive for the micromotion magnitude at the stem–neck interface of bi-modular hip implants, *Medical Engineering & Physics* 36 (2014) 300–307.
- [34] M. Baxmann, S.Y. Jauch, C. Schilling, W. Blömer, T.M. Grupp, M.M. Morlock, The influence of contact conditions and micromotions on the fretting behavior of modular titanium alloy taper connections, *Medical Engineering & Physics* 35 (2013) 676–683.
- [35] DLC coating deposition machine TSD 550, from HEF.  
[http://www.tshungary.hu/dok/DLC\\_coating\\_equipment.pdf](http://www.tshungary.hu/dok/DLC_coating_equipment.pdf)
- [36] I.N. Sneddon, The relation between load and penetration in the axisymmetric boussinesq problem for a punch of arbitrary profile, *International Journal of Engineering Science* 3 (1965) 47–57.
- [37] P. Zhang, S.X. Li, Z.F. Zhang, General relationship between strength and hardness, *Materials Science and Engineering A* 529 (2011) 62–73.
- [38] Y.X. Leng, J.Y. Chen, P. Yang, H. Sun, N. Huang, Structure and properties of passivating titanium oxide films fabricated by DC plasma oxidation, *Surface and Coatings Technology* 166 (2003) 176–182.
- [39] A.F. Yetim, Investigation of wear behavior of titanium oxide films, produced by anodic oxidation, on commercially pure titanium in vacuum conditions, *Surface and Coatings Technology* 205 (2010) 1757–1763.